Sensors and Materials, Vol. 34, No. 11 (2022) 4137–4156
MYU Tokyo

S & M 3102

Linear Axial Error Signal Measurement and Processing Method of a Machine Tool for Accuracy Compensation Improvement

Kun-Ying Li,[1*] Meng-Chiou Liao,[2] and Swami Nath Maurya[3]

[1]Department of Intelligent Automation Engineering, National Chin-Yi University of Technology, No. 57, Sec. 2, Zhongshan Rd., Taiping Dist., Taichung 41170, Taiwan
[2]Department of Mechanical Engineering, National Chin-Yi University of Technology, No. 57, Sec. 2, Zhongshan Rd., Taiping Dist., Taichung 41170, Taiwan
[3]Graduate Institute of Precision Manufacturing, National Chin-Yi University of Technology, No. 57, Sec. 2, Zhongshan Rd., Taiping Dist., Taichung 41170, Taiwan

(Received June 4, 2022; accepted November 1, 2022)

Keywords: linear axial, signal processing, accuracy compensation, machine tool

With the rapid development of electronics, sensors, wireless communication, networks, and software, machine tool (MT) technology has entered a period of intelligentization in industry. As a result, experiential knowledge relying on domain experts will gradually be substituted by intelligent technology. The accuracy of MTs can be upgraded by reducing the human experience effectively. However, when dynamic errors resulting from the motion of MTs induce abnormally large composite accuracy errors, the errors must be removed by shutting down the MT or handled by periodic preventive maintenance. These processes are time-consuming and costly, and shutdown inspections affect a factory's production cycle and productivity. In this study, an accelerometer was integrated with a gyroscope to create an inertial measurement unit used to measure the accuracy error in the dynamic behaviors of MTs. The measured vibration signals of the acceleration and angular acceleration were processed by the basic mathematical operations of filtering and integration, and the subsequent values were merged using the data fusion method to remove the information and errors resulting from repeated integrations or cumulative frequencies of blended data. Finally, the accuracy errors of the MT and angle value errors were obtained with high reliability in this study. In an experiment to validate the accuracy of the signal measurement and processing of the constructed inertial measurement unit module, a movable table of MTs was tested under compensation error baselines of 15 and 50 μm. In the case of 10 mm travel, the positioning value was increased by 5.58 μm under 15 μm testing and reduced by 2.34 μm under 50 μm testing. According to the measurement and operation, the inertial measurement unit block conformed to the principle of the measuring tool unit being at least 0.2–0.5 times the compensation unit, and the validation results matched the target.

1. Introduction

With the rapid development of electronics, sensors, wireless communication, networks, and software, machine tool (MT) technology has entered a period of intelligentization in industry, in

*Corresponding author: e-mail: likunying@ncut.edu.tw
https://doi.org/10.18494/SAM4152

ISSN 0914-4935
https://myukk.org/

which experiential knowledge depending on domain experts will be gradually substituted by intelligent technology. The accuracy of MTs can be upgraded by reducing the human experience effectively. However, when dynamic errors resulting from the motion of MTs induce abnormally large composite accuracy errors, they must be removed by shutting down the machine or handled by periodic preventive maintenance. These processes are time-consuming and costly, and shutdown inspections affect a factory's production cycle and productivity.[1,2]

The manufacturing industry has experienced rapid increases in labor shortage and labor cost. As the concept of smart manufacturing becomes widespread, lights-out production and unstaffed factories[3–6] are slowly becoming a trend in the industry. The spirit of Industry 4.0 is connection and optimization, linking manufacturing-related elements for optimization to improve the competitiveness and profits of businesses. In practice, when the accuracy and reliability of machine tools in terms of temperature, vibration, and control fail to meet requirements,[7,8] the implementation of lights-out factories will be an issue. The linear axial precision of an MT significantly affects the accuracy of manufactured parts. In the working of MTs, faults in the linear axial system reduce precision and reproducibility.[9] Vogl *et al.*[10] mentioned that the linear axial system is one of the important subsystems of an MT; when the linear axial system degrades, the overall system productivity degrades accordingly. In their study, changes in the linear and angular errors of a linear axial system were found using the data of an inclinometer, an accelerometer, and a gyroscope. Szipka *et al.*[11] employed an inertial measurement unit (IMU) to evaluate the accuracy failure variations of two linear axes of an MT for MT accuracy compensation control, and the measured accuracy error resulted in a linear axial accuracy error variation without a double integral, in contrast to the conventional measuring method.

The accuracy of an MT is usually obtained through signal processing, and how to obtain the best accuracy results is very important. Although different signal processing methods have different final accuracy values, most of the multitarget signal processing methods utilize data fusion to optimize the signal results. Coraluppi and Carthel[12] proposed the multiple hypothesis tracking (MHT) algorithm for multitarget signal tracking problems and used an approximate method to validate the final signal processing result. Their result showed that the MHT method can directly treat signal problems by target aggregated Kalman filtering to significantly enhance the reliability of the signals. However, Rincon *et al.*[13] indicated that a particle filter is more flexible than the Kalman filter, as it can handle the nonlinear dependence and non-Gaussian density in dynamic models and noise errors. However, many particles are needed to achieve a modest variation in estimation, and the computational cost is decreased. To reduce the computational cost of particle filters and enhance the reliability of signals, distributed particle filters[14–16] have been extensively used. Coates[15] used a dispersed particle filter to detect the surroundings of space models and obtained a nonlinear signal result and non-Gaussian noise. Morbee *et al.*[17] used the Dempster–Shafer theory to construct a 2D view with multiple cameras and evaluated the contribution of each camera to the task. Their primary objective was to evaluate the effectiveness of fusion hypotheses using the Dempster–Shafer theory.

In contrast, most optimal statistical methods require a significant amount of computing, and their sophistication typically rises exponentially with the number of objectives. When a particle filter is used, multiple target signals can be acquired simultaneously as a combination. However,

if multiple target signals are monitored simultaneously, the required number of particles increases exponentially. Compared with a particle filter, the distributed data fusion method has several advantages in data fusion. Castanedo and coworkers[18,19] used the inherent redundancy of distributed systems and found that the complexity of particle filters can be reduced by using distributed inference techniques and collaborative calculations. Davenport *et al.*[20] proposed a simple model that could obtain the correlations among the measured values of sensors by matching different parameter values.

An IMU module for MT equipment accuracy error measurements was built and designed in this study. The mathematical operation of the acceleration and angular acceleration in the dynamic procedure was combined with data fusion to obtain the displacement and angle values with high reliability. The corresponding axial feed rate and optimum bandwidth were fused with the spatial frequency so that real-time error identification and self-compensation control functions may be developed in the future.

2. Construction of Experimental Equipment

2.1 Experimental equipment and IMU system

In this study, an IMU accuracy measurement module with an accelerometer and a gyroscope was built and designed. The sensing elements included chips for the accelerometer, gyroscope, microcontroller unit (MCU) control, and power management, which were used to capture and analyze the signals. A three-axis vertical computer numerical control (CNC) MT was set up, and the IMU measurement module was installed on a moving table. The moving table reciprocated backward and forward, and the measured linear acceleration and angular velocity were quickly retrieved, as shown in Fig. 1. The measured values were then converted using various functions (the acceleration was converted into the displacement, and the angular velocity was converted

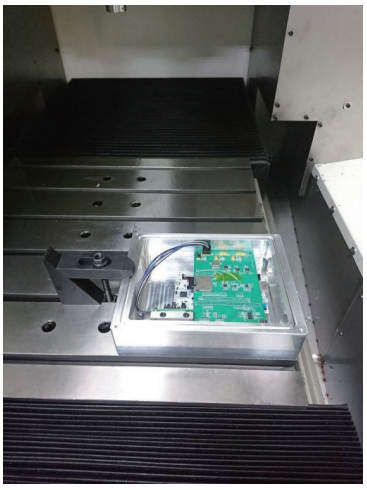

Fig. 1. (Color online) Three-axis vertical CNC MT and measurement installation.

into an angle). The high-frequency and low-frequency data were analyzed by fusing the data of the corresponding axial feed rate and optimum bandwidth with the spatial frequency to obtain the axial displacement and angle.

Figure 2 shows the accuracy measurement module, comprising an MCU control board, a sensing module board, and an outer casing. The STM32H7 MCU control board used a 480 MHz Cortex-M7 kernel, which has the highest efficiency of the ARM Cortex-M series. An additional 240 MHz Cortex-M4 kernel was used to provide a running frequency of 480 MHz, making it suitable for high-speed floating-point operations.

According to the design specifications of the STM32H743ZIT6 board, a pin-to-pin abutment sensor module board was designed to capture and process signals. This sensor board includes an SD card interface that can be inserted into an SD card to store all measurement signals, a three-axis accelerometer used to capture the vibration signal, a gyroscope, and a differential signal analysis IC used to capture the angle error signal. A total of three connectable channels for differential signals were maintained, with one connected to a low-frequency high-sensitivity SDI 1521 accelerometer. The SD card could reach a reading speed above 32000 Hz during signal transmission. Table 1 shows the sensor specifications.

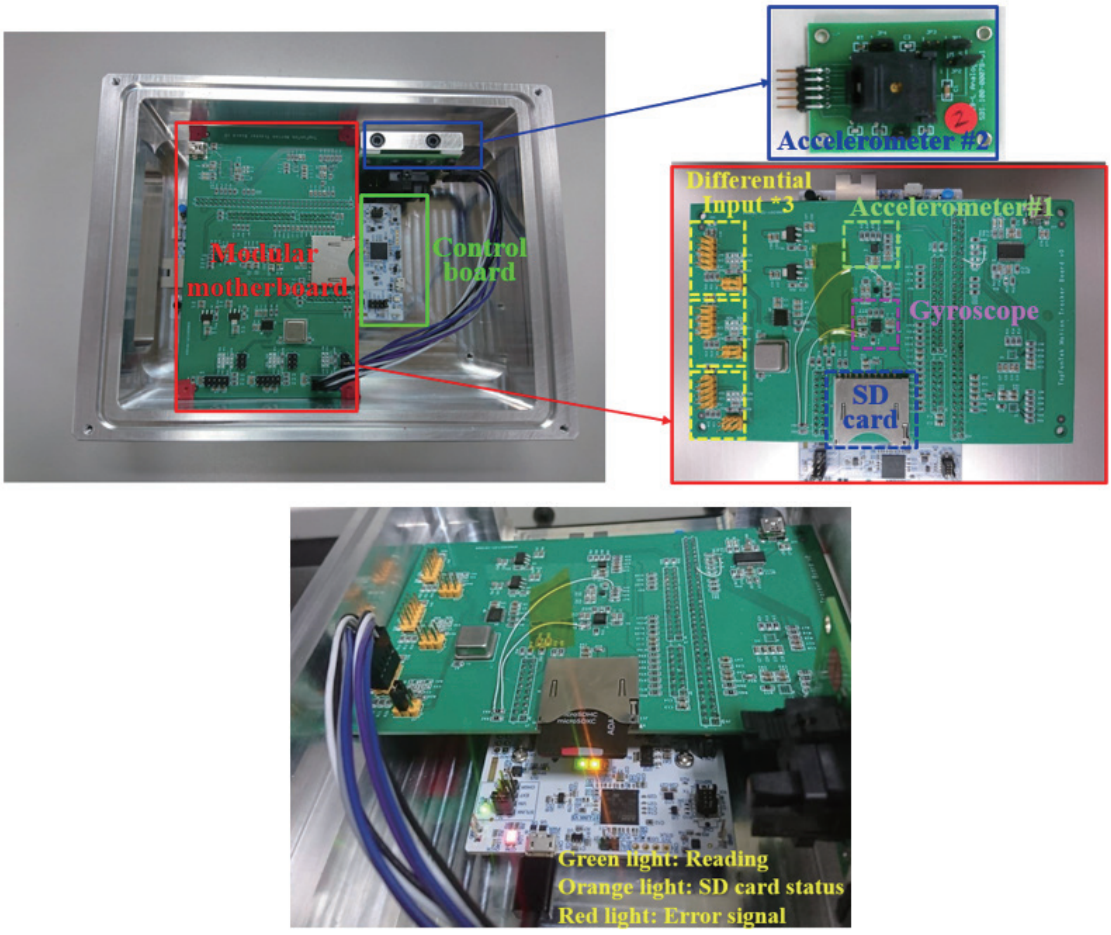

Fig. 2. (Color online) IMU accuracy measurement module.

Table 1
Sensor specifications.

Sensor	Product	Bandwidth (Hz)	Noise
Accelerometer 1	SDI 1521-002	400	5 (μg/s)/√Hz
Accelerometer 2	AIS328DQ	500	218 (μg/s)/√Hz
Rate gyroscope	L3GD30H	50	1.919 (mrad/s)/√Hz

2.2 Research theory

An IMU measurement module with an accelerometer and a gyroscope was used for accuracy error measurements in this study. The acceleration values in the linear axial system motion of an MT and the angular velocity of rotation were measured using the accelerometer and gyroscope, respectively. Integral computations were used to collect information about the linear system's speed, location, and angular variations. According to Newton's second law of motion, the value estimated using an accelerometer corresponds to a particular force. Thus, the equation of motion in the inertial coordinate system (i) can be expressed as

$$f^i = \ddot{r}^i - G^i, \tag{1}$$

where f^i is the specific force vector, $\ddot{r}^i$ is the particle acceleration vector, and G^i is the gravitational acceleration vector.

The uniaxial accelerometer system was a second-order dynamic mass–spring–damper system expressed as

$$\ddot{x} + \frac{c}{m} \cdot \dot{x} + \frac{K_x}{m} \cdot x = -\left(\ddot{r} - G\right), \tag{2}$$

where c is the damping constant, m is the inertia mass, x is the change in spring length, K_x is the spring stiffness coefficient, and $\ddot{r} - G$ is the specific force. In this analysis, the gyroscope was employed to evaluate the angular velocity of the system. The second-order dynamic system can be expressed as a second-order ordinary differential equation:

$$I_0\ddot{\theta} + b\dot{\theta} + k_{tb}\theta = H\Omega, \tag{3}$$

where I_0 is the moment of inertia, b is the damping constant, k_{tb} is the rotational stiffness, θ is the angle, and Ω is the angular velocity.

The speed signal (primary integral) and displacement (quadratic integral) can be derived from integral operations of acceleration signals, and the double integral is expressed as

$$\int_0\int_0^{\tau} f(x)dxd\tau, \tag{4}$$

where t is the time and τ is the time constant.

2.3 Research method

As shown in Fig. 3, data fusion was used to estimate the straightness error. We used the data fusion method to decompose the steady-state signal generated by the same geometric defect into components of various frequencies, and we reconstructed the original error signal by the recombination of signal filters. The operating speed and tracking length ranges of the MT, velocities of 40 and 16 mm/s were chosen, and the filter was divided according to the main signal frequencies of 20 and 350 Hz obtained by frequency analysis to obtain the geometric error that could be most stably detected at different speeds while retaining a consistent spatial frequency. The results of this study indicated that the acceleration frequency domain diagrams generated at various speeds would have a higher reproducibility in their specific temporal frequency blocks. Therefore, the data fusion method could convert the temporal frequency into

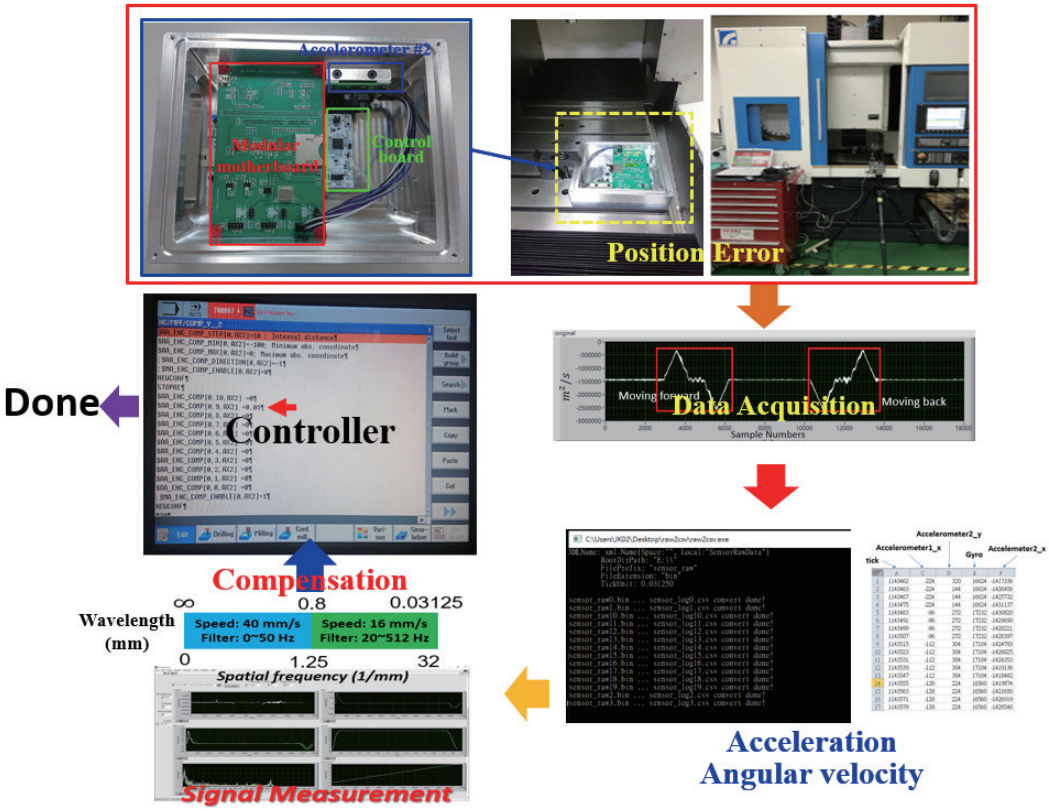

Fig. 3. (Color online) Research method.

the spatial frequency domain corresponding to the rate of movement, and various signals could be merged by frequency filtering without affecting the consistency of the spatial frequency.

To evaluate signal reproducibility, according to the operating velocity and tracking length ranges of the MT, velocities of 40 and 16 mm/s and two main signal frequencies of 20 and 350 Hz were selected. The objective was to obtain the most stable geometric error that can be detected at different speeds while maintaining a consistent spatial frequency.

3. Results and Discussion

To directly display the machine accuracy results to the user, an HTCU11 smartphone with a built-in Bosch BMA 253 sensor (G-sensor) was used as the sensing device. The noise processing result and reproducibility were better than the results of simply using the sensor with the JN5168 microcontroller as the core substrate to validate the integrated MAX21105 six-axis IMU sensor. At different feed rates, the numerical error reproducibility at a constant high speed (10 m/min) and a constant low speed (3 m/min) was higher than 3%, but significant differences were observed under different traveling speeds, showing the importance of coordinating the noise processing, accelerometer bandwidth, and resolution.

3.1 Module signal capture

In this study, data acquisition had to avoid data loss when the moving table was running at a high speed. However, when the amount of data increases at a high speed, the computational complexity increases and data transmission congestion occurs. Thus, the SD card storage was designed as another signal capture channel. The serial port transmission rate of the SD card on the module was 10 MB/s and the frequency was 32 kHz during single-channel signal reading. The writing activity was monitored via the COM port while writing to the SD card, as shown in Fig. 4.

The USB module connection only provided an external power supply instead of monitoring the system; however, the user could identify the system state according to the three IO light signals on the board, as shown in Fig. 2. The orange light signaled the need to check whether the SD card was correctly installed. The green light indicated the reading state, meaning that the system was capturing information. The red light was the error signal; common errors included the SD card being full of files or an input error occurring when the memory card was removed during reading. In addition, to implement high-speed data acquisition, raw data was chosen to input the SD card instead of strings. Therefore, the data in the SD card could not be directly opened; rather, it needed to be decoded into comma-separated value (CSV) files for subsequent software reading and calculation, as shown in Fig. 5.

Plotting the accelerometer measurements in the *Z*-axis from the CSV data yielded Fig. 6. As shown in Fig. 6(a), the two signals had good concurrency, and the low-frequency high-sensitivity SDI accelerometer was characterized by low noise and response. The module was placed on the MT for reciprocation. Figure 6(b) shows that the general accelerometer had relatively obvious noise interference in the constant-acceleration and zero-speed regions, whereas the SDI had a relatively good signal-to-noise ratio in these regions.

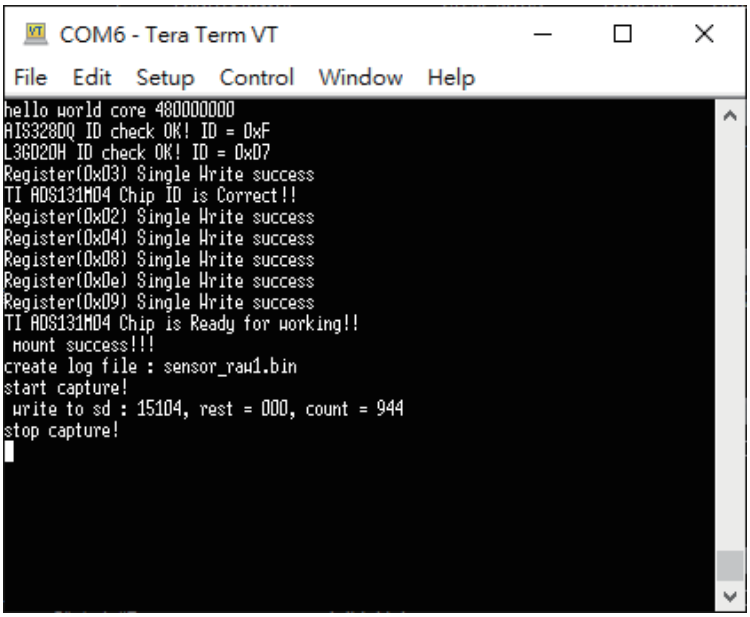

Fig. 4. (Color online) Measurement signal access by SD card.

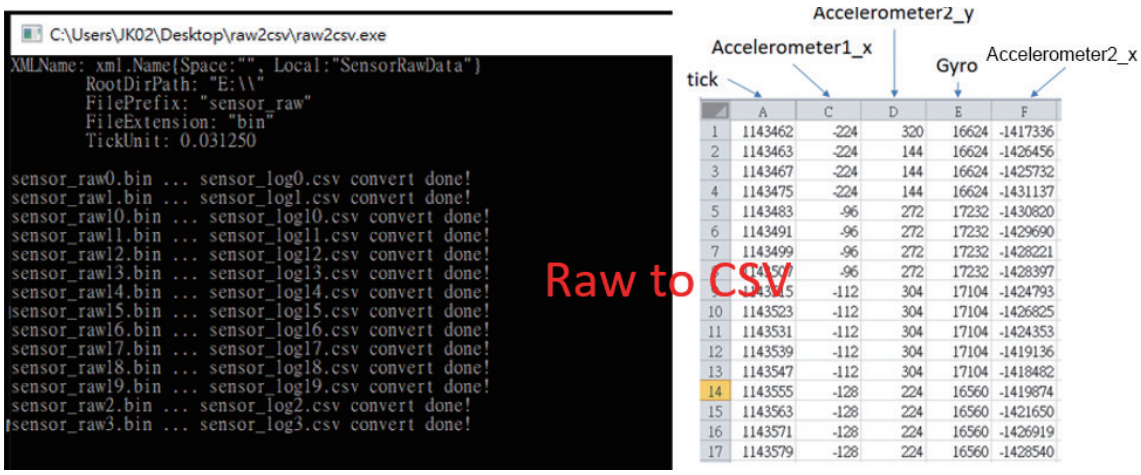

Fig. 5. (Color online) Raw data to CSV conversion.

3.2 Signal processing

The signals corresponding to the reciprocating motion of the IMU module on the MT are shown in Fig. 7(a). In the motion axes, the origin of the coordinates was not zero in the stationary state, because the signal data were formatted without positive or negative signs, and the sensor

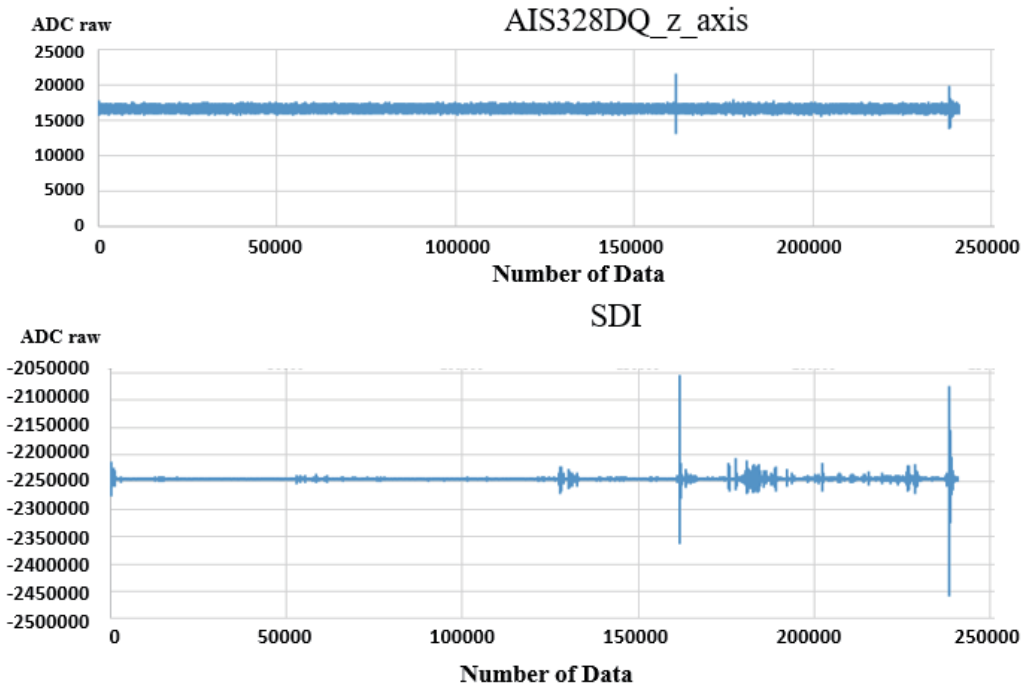

(a)

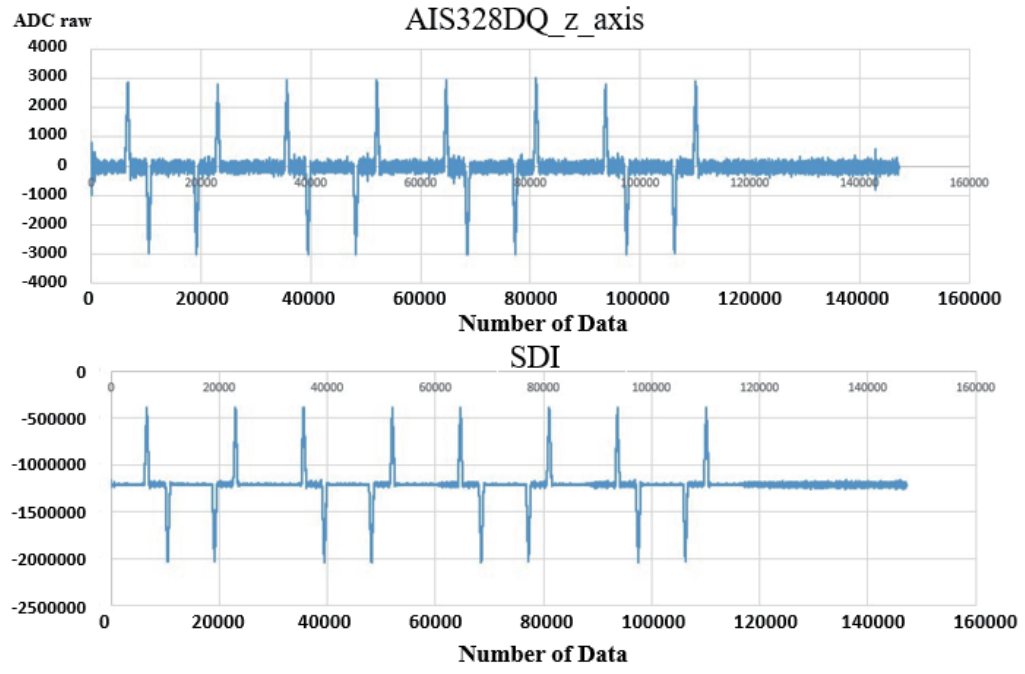

(b)

Fig. 6. (Color online) Comparison of accelerometer signals: (a) comparison between the two accelerometers and (b) actual machine test.

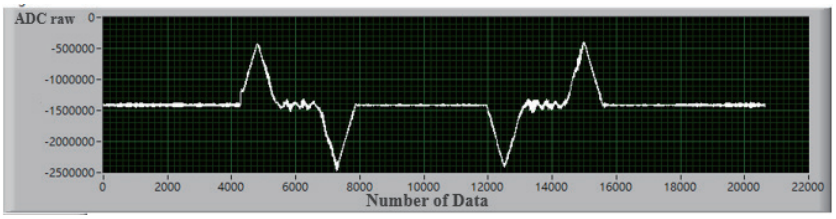

(a)

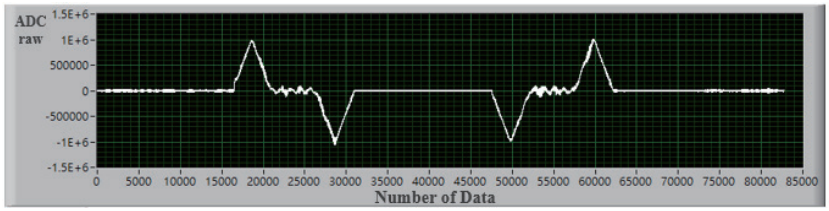

(b)

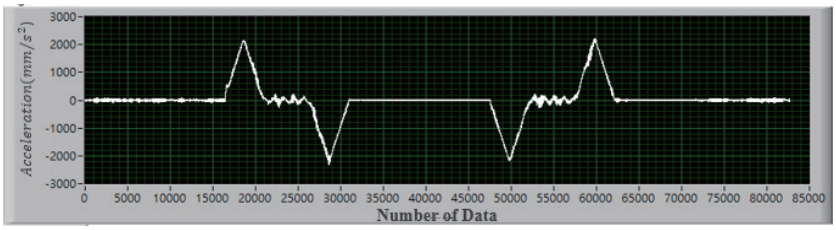

(c)

Fig. 7. (Color online) Normalized data: (a) original signal, (b) signal origin offset, and (c) converted correct unit.

signals were free of zero correction. A stagnant zone was set as zero during zero correction, and the entire segment of signals was numerically displaced. An image of the numerical displacement is shown in Fig. 7(b); at this time, the stagnant or uniform acceleration zone approached the return-to-zero value of the *y*-axis. Finally, it was necessary to confirm the units of the values before the track could be calculated. The *x*- and *y*-axes were mapped into the correct format according to the sensor acceleration, voltage conversion, and tick frequency, as shown in Fig. 7(c).

The test stroke included the outbound motion, return motion, and several lengths of rest time. When the interval with movement was extracted and calculated during trajectory analysis, the accumulated errors in the integral were reduced. The acceleration variation was used as a feature value, and the acceleration and deceleration regions were marked. The sensing region of interest (ROI) was labeled according to the NC running-in rule and cut out of the original diagram for path tracking. Figure 8 shows the cutting process of the table moving from $y = 0$ to -200 mm, including the initial acceleration, followed by motion at a constant speed and deceleration to a stationary state.

In the process of signal acquisition using the accelerometer, in addition to the motion signal, there are also transient errors caused by the environment noise. The 20 sets of data were overlapped to analyze them, and it was found that although the signals of the movement process were consistent, there were unstable noise deviations in the segment. As shown in Fig. 9(a), the 20 sets of data overlap. The signals from the same motion showed consistency but had uncertain noise deviations in some zones, which was due to a transient error that did not continuously occur in the same motion. To reduce the effect of transient errors on the motion accuracy, the signals were overlapped and numerous signals were averaged to reduce the effect of noise without reproducibility. Figures 9(b) and 9(c) show the averages of five and 20 sets of data, respectively. According to the experiment, the average curve converged after about 20 sets of data. In other words, averaging more signals is not helpful for improving the data convergence.

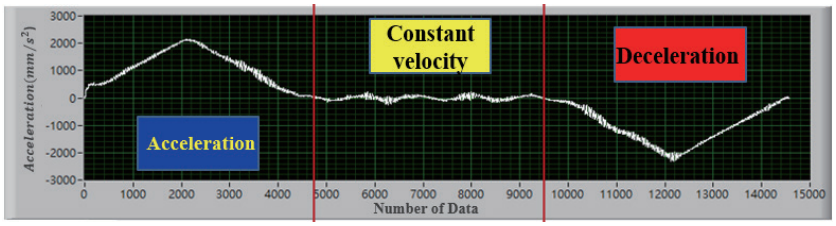

Fig. 8. (Color online) Signal cutting results.

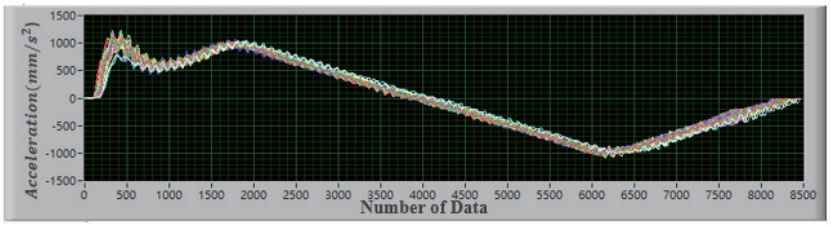

(a)

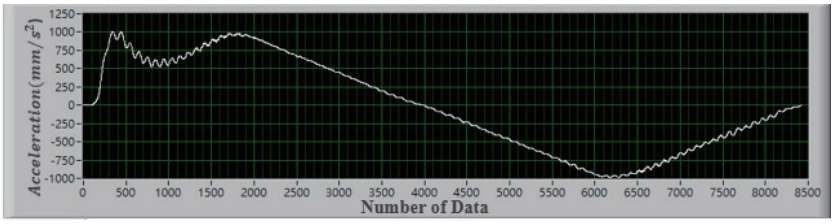

(b)

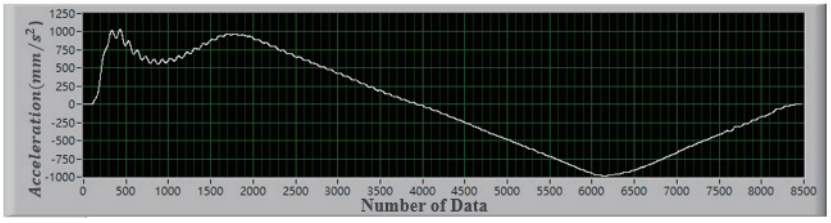

(c)

Fig. 9. (Color online) Transient error: (a) superposed signals, (b) average of five sets of data, and (c) average of 20 sets of data.

In the trajectory operation, the acceleration was integrated with respect to the time unit to obtain the velocity diagram and integrated again to obtain the displacement diagram. The moving table traveled in the range of y = 0 to 200 mm, and the running velocity was set as 320 mm/s, 80% of 400 mm/s. Figure 10(a) shows that the velocity in the constant-velocity region was about 320 mm/s. Figure 10(b) shows that the final displacement was 200 mm. Displacements of 10, 100, and 200 mm were tested, and the locations of the final points of the cumulative displacement diagrams matched the running-in settings of 10, 100, and 200 mm.

The data measured using the gyroscope were the angular velocity, similar to the displacement calculated using the accelerometer; however, the angular displacement calculation only required one integral. In addition, in the preprocessing signal cutting, when the moving table had a linear displacement, the variation in angular velocity was small, making it difficult to find the distance of table movement from the variation in angular velocity. Figure 11 shows that the angular velocity signal was cut according to the synchronous signals, and the signal measured using the accelerometer on the module board changes significantly. The resulting angular displacement was obtained from the primary integral of the angular velocity cutting result. Finally, by the superposition analysis of the results of multiple angular velocity experiments, we found that the numerical variation in angular displacement at the end of the run was 0.0429 mm. The results show that the gyroscope on the IMU module can be used for angular positioning. However, a lower frequency sensor is required to achieve μm-scale angular displacement longitude compensation. An angular velocity meter with differential signal outputs can be used to enhance performance in the future.

To achieve optimal monitoring accuracy, we discuss the frequency domain distribution during running-in. Figure 12 shows the acceleration frequency domain diagram for 80 mm/s running-in motion. There were two obvious sets of peak amplitudes at 0–40 and 200–400 Hz. From the results of frequency analysis, it was found that for the moving distance of the

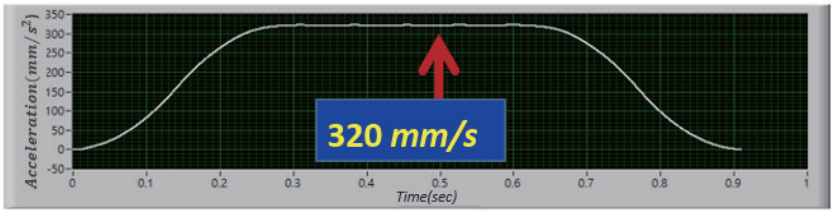

(a)

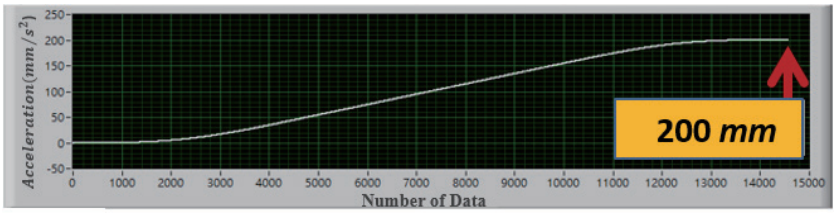

(b)

Fig. 10. (Color online) Trajectory operation: (a) velocity diagram and (b) displacement diagrams.

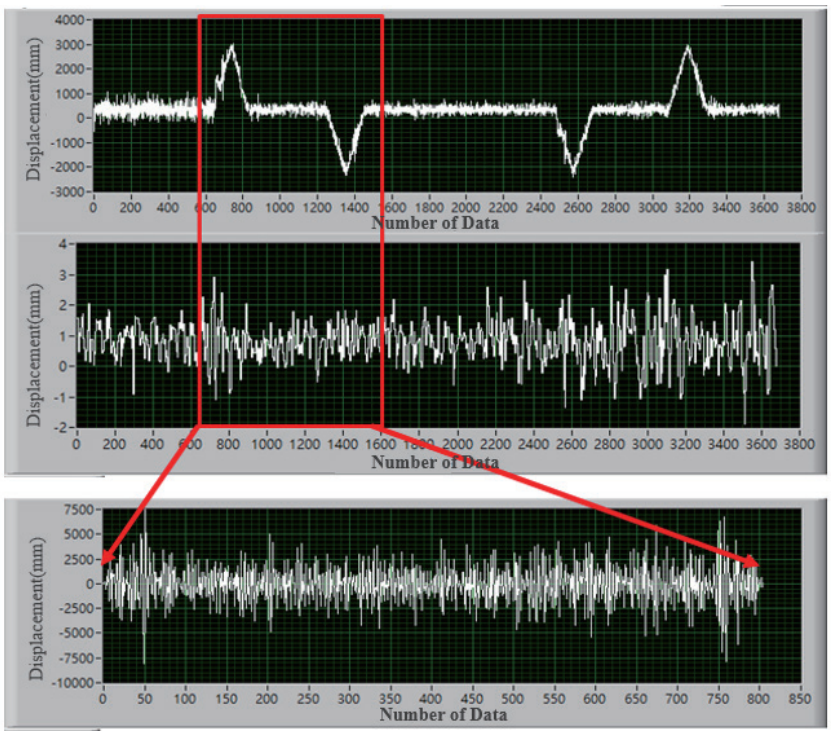

Fig. 11. (Color online) Gyro signal cutting.

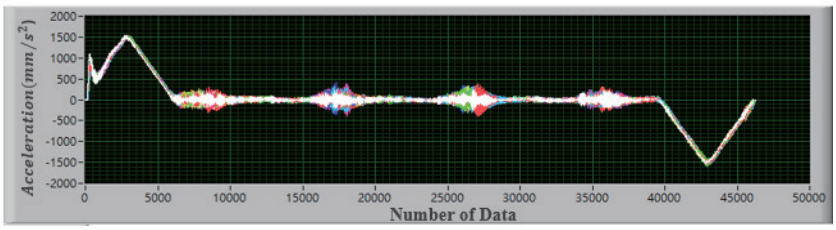

(a)

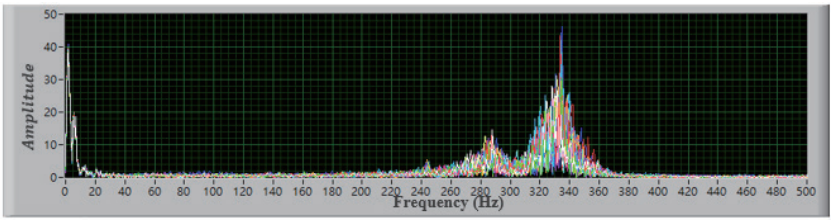

(b)

Fig. 12. (Color online) (a) Acceleration and (b) frequency domain diagrams for medium-speed running-in at 80 mm/s.

experiment, the vibration generated by the acceleration was mainly concentrated at 0–40 and 200–400 Hz.

To clarify the relationship between the two frequency bands and the running-in motion, the frequency domain diagrams of two other speeds were analyzed, as shown in Figs. 13 and 14. In the motion at the higher speed of 320 mm/s (Fig. 13), the amplitude energy was concentrated at

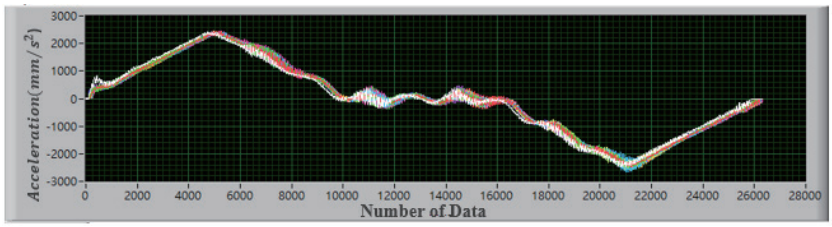

(a)

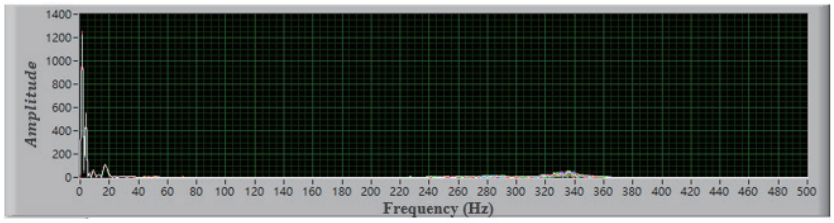

(b)

Fig. 13. (Color online) (a) Acceleration and (b) frequency domain diagrams for high-speed running-in at 320 mm/s.

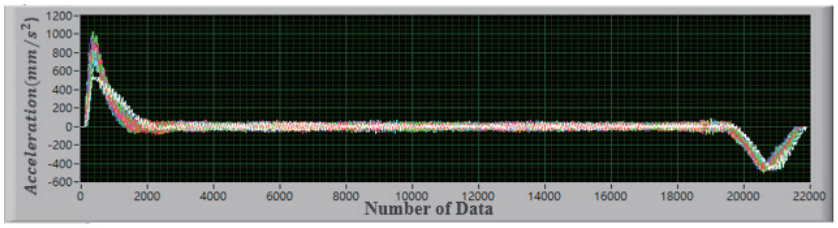

(a)

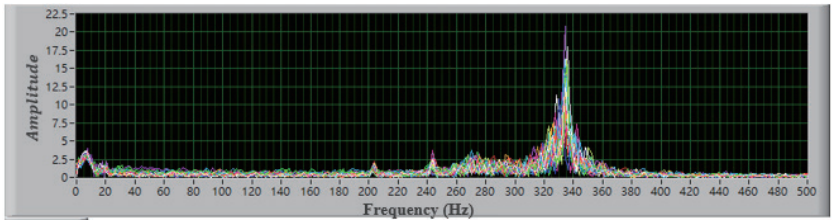

(b)

Fig. 14. (Color online) (a) Acceleration and (b) frequency domain diagrams for low-speed running-in at 16 mm/s.

0–40 Hz and had high reproducibility, and the amplitude variation at 350 Hz was greatly reduced.

The frequency domain diagram of the motion at the low speed of 16 mm/s is shown in Fig. 14. The amplitude energy was concentrated at 180–400 Hz, and the low-frequency signals almost disappeared. The amplitude at 180–400 Hz had a higher reproducibility than the medium-speed motion. Therefore, to evaluate the steady-state signals, it was necessary to simultaneously observe the low-frequency band (about 20 Hz) of the high-speed motion and the high-frequency band (about 350 Hz) of the low-speed motion.

The data fusion method was used to evaluate straightness errors in this study. The steady-state signal generated by a geometric error was subdivided into different elements with various frequencies, and the original error signal was then generated by recombining the filtered signals. In terms of the spatial frequency, different sensor signals generated the same geometric error in adjacent spatial frequency ranges. As mentioned above, the acceleration frequency domain diagrams for different speeds had a higher reproducibility in specific temporal frequency blocks. Therefore, various signals could be combined by frequency filtering without affecting the consistency of the spatial frequency provided that the temporal frequency could be converted into the spatial frequency domain corresponding to the moving speed.

Similarly to when evaluating the signal reproducibility, the operating speeds of the MTs were chosen to be 40 and 16 mm/s. The filter was divided according to the main signal frequencies of 20 and 350 Hz obtained by frequency analysis. Our objective was to obtain the most stable geometric error that can be detected at different speeds while maintaining a constant spatial frequency, as shown in Fig. 15.

3.3 IMU module validation

In the experiment, the IMU module was placed on the moving table of the MT, the correct start of the signal result was tested, and related data were captured. The machine tool makes the table move in an axial reciprocating manner by the action commands of the controller; the travel distance was 10 mm and the back-and-forth movement was performed 20 times. The traveling speeds used to find the reproducibility of the localization accuracy after the movement of the moving table were a lower speed of 16 mm/s and a higher speed of 40 mm/s. In the experimental

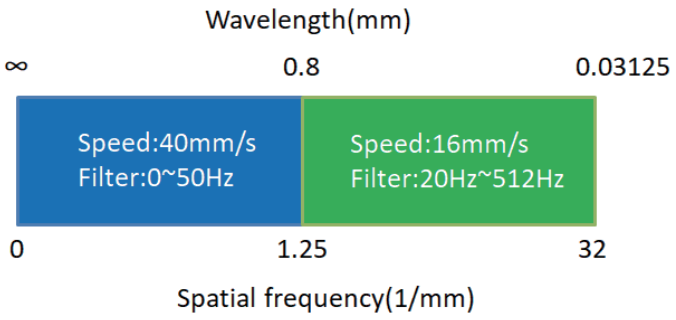

Fig. 15. (Color online) Spatial frequency distribution.

process, the acceleration signal was directly recorded in the SD card in the IMU module, and the experimental positioning information was found by computer calculation. The error value tested in the indicated spatial frequency domain was found to have good reproducibility. The moving table of the MT was then set up under error baselines of 15 and 50 μm for validation testing and compensation. The actual result after the axial accuracy compensation of the movement was thus obtained.

First, the moving table at a traveling speed of 16 mm/s was tested, and the outward signal was recorded. As shown in Fig. 16, the displacement error calculation result was obtained by integrating the acceleration signals twice after bandpass filtering at 20–512 Hz. Figure 16(a) shows the signals of the reciprocation motion on the moving table; the sampled data were 3,600 to 6,400 outbound signals, and the acceleration, speed, and displacement were obtained by integration. Figure 16(b) shows the displacement of the moving table obtained after integrating the experimental signals twice. The displacement was tested 20 times at a traveling speed of 16 mm/s, and the standard deviation was calculated to verify the high consistency of the experimental method. The calculated processing displacement was the displacement variation of

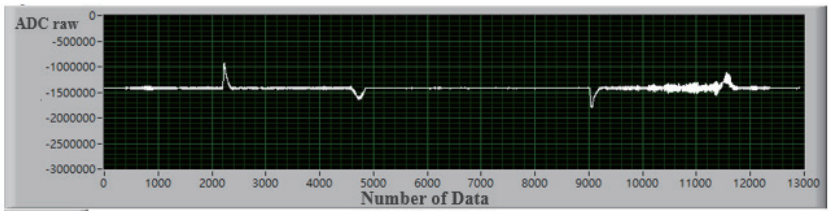

(a)

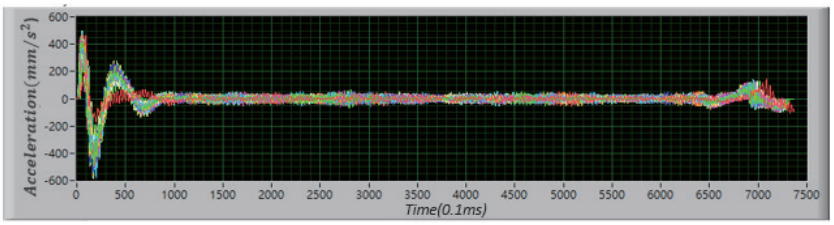

(b)

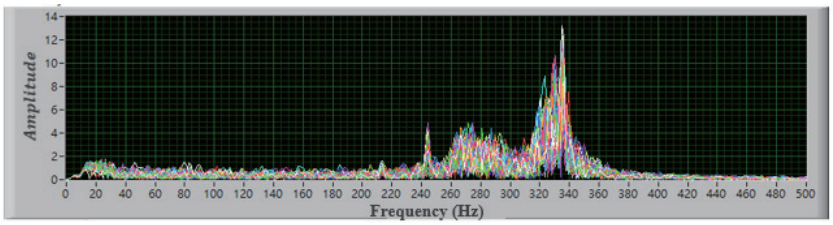

(c)

Fig. 16. (Color online) Low-speed signal measurement results: (a) low-speed reciprocation signal, (b) low-speed signal overlay after filtering, and (c) low-speed frequency domain signal.

the short-wavelength zone in the spatial frequency, but the real displacement error caused by the mechanical structure was the entire displacement error of the uninterrupted wavelength signals encompassing the short-wavelength and long-wavelength zones. Figure 16(c) shows the frequency domain signal resulting from filtering the low-speed signals obtained in experiments. The calculated cumulative variation was 0.007959 mm and the standard deviation of the numerical error was 0.029 μm, demonstrating the high consistency of the IMU module at a low speed of 16 mm/s.

The moving table at a traveling speed of 40 mm/s was tested, and the outward signal was recorded. Figure 17 shows that the error calculation result was obtained by evaluating two integrals after bandpass filtering at 20–512 Hz. Figure 17(a) shows the signals of the reciprocation on the moving table; the sampled data were 3000 to 6200 outbound signals, and the acceleration, speed, and displacement were obtained by integration. Figure 17(b) shows the displacement of the moving table resulting from two integral operations of the experimental signals. The

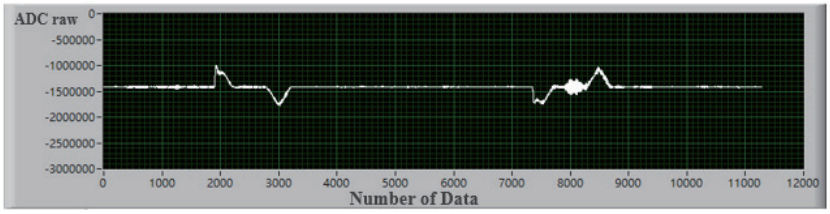

(a)

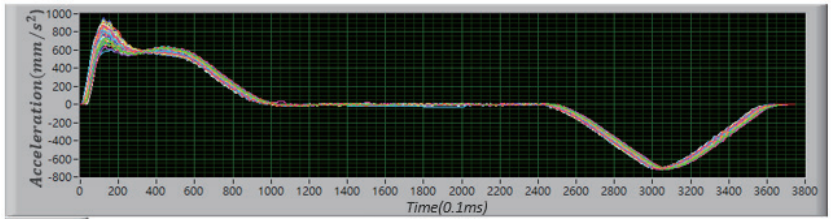

(b)

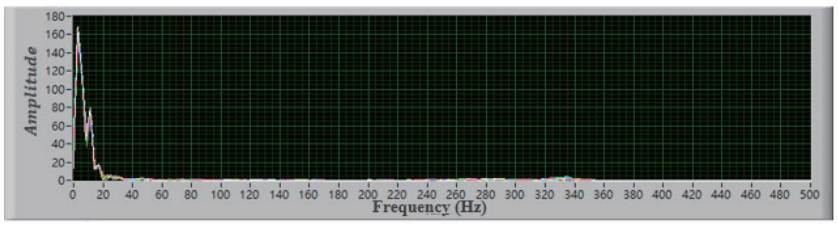

(c)

Fig. 17. (Color online) High-speed signal measurement results: (a) high-speed reciprocation signal, (b) high-speed signal overlay after filtering, and (c) high-speed frequency domain signal.

Table 2
Experimental validation results.

Offset (μm)	Axial motion velocity (mm/s)		Location result (mm)	Relative offset (μm)	Error (μm)
	16	40			
0	0.00801	10.01539	10.0234	0	0
15	0.00808	10.0359	10.04398	20.58	5.58
50	0.00811	10.06295	10.07106	47.66	2.34

displacement was tested 20 times at a traveling speed of 40 mm/s, and the standard deviation was calculated to verify the high consistency of the experimental method. The calculated processing displacement was the displacement variation of the short-wavelength zone in the spatial frequency, but the real displacement error caused by the mechanical structure was the entire displacement error of the uninterrupted wavelength signals from the short-wavelength and long-wavelength zones. Figure 17(c) shows the frequency domain signal resulting from filtering the high-speed signals. The calculated cumulative variation was 9.9325 mm and the standard deviation of the numerical error was 5.053 μm, demonstrating the reproducibility of the IMU module at a high speed of 40 mm/s. The low-speed and high-speed positioning values were added during signal fusion, and the standard deviation of the error was 5.053 μm + 0.0029 μm ≈ 5.0 μm.

A positioning error compensation experiment was performed to validate the measurement accuracy of the IMU module. The compensation value was set at 15 and 50 μm by the MT controller, and the axial movement of the moving table was set at 10 mm. In the 10 mm axial movement, after the measurement of the IMU module and calculation, the correct actual physical space and compensation were 10.015 and 10.05 mm, respectively. Table 2 shows the measurement results after compensation. The positioning result was 10.0234 μm prior to compensation. After 15 and 50 μm positioning compensations, the positioning values were 20.58 and 47.66 μm, respectively. Comparing these values with 15 and 50 μm, the positioning value below 15 μm showed an increase of 5.58 μm, and the positioning value below 50 μm showed a reduction of 2.34 μm. The measurement and operation results of the IMU module met the requirement that the measuring tool unit must be at least 0.2–0.5 times the compensation unit. The validation results therefore achieved the target.

4. Conclusions

According to the experimental measurements of the IMU module, the accuracy of the positioning error could be controlled at 5 μm/m. However, the geometric error was only tens of μm because the acceleration signal was acquired by signal cutting using the thresholds of the reciprocating motion and the acceleration variation of the moving axis. Moreover, angular velocity signal cutting was defined by the acceleration cutting range. When the acceleration signal cutting range differed from the real physical movement, the signal acquisition range of the angular velocity accumulated errors. Therefore, the verification result of the geometric error was inferior to that of the positioning error. In future studies, the position signals of the MT controller should be combined with the acceleration and angular velocity signals to make a signal pattern

that can solve the cumulative error problem of angular velocity and accurately obtain the acceleration and angular velocity signals at every position of every controller. By calculating the positioning and geometric errors for every position, the ideal geometric error measurement accuracy can be achieved. The module can be combined with remote equipment precision monitoring and health recording systems in the future to assist autonomous prognoses and equipment control.

Acknowledgments

The authors gratefully acknowledge the financial support provided by the Ministry of Science and Technology of Taiwan under Grant MOST 110-2222-E-167-001-MY3.

References

1 TCO SAVING: http://www.anger-machining.com/en/solutions/tco-saving/ (accessed 2018).
2 Industrial Temperature Control Services — Market Drivers and Growth Prospects | Technavio: https://www.businesswire.com/news/home/20171019005991/en/ (accessed 2017).
3 J. R. Meredith: J. Manuf. Syst. **6** (1987) 1. https://doi.org/10.1016/0278-6125(87)90045-8
4 A3 ROBOTICS: https://www.robotics.org (accessed 2017).
5 P. Grefen, I. Vanderfeesten, K. Traganos, and Z. Domaglal-Schmidt: Machines **10** (2022) 45. https://doi.org/10.3390/machines10010045
6 P. Brödner: Int. J. Ind. Ergon. **1** (1986) 145. https://doi.org/10.1016/0169-8141(86)90018-1
7 Lubrication FMEA: The Big Picture: https://reliabilityweb.com/articles/entry/lubrication_fmea_the_big_picture/ (accessed 2018).
8 K. Y. Li, W. J. Luo, X. H. Hong, S. J. Wei, and P. H. Tsai: IEEE Access **8** (2020) 28988. https://doi.org/10.1109/ACCESS.2020.2972580
9 Y. Li, X. Wang, J. Lin, and S. Shi: Sensors **14** (2014) 2071. https://doi.org/10.3390/s140202071
10 G. W. Vogl, M. Calamari, S. Ye, and M. A. Donmez: Procedia Manuf. **5** (2016) 621. https://doi.org/10.1016/j.promfg.2016.08.051
11 K. Szipka, A. Archenti, G. W. Vogl, and M. A. Donmez: CIRP Ann. **68** (2019) 547. https://doi.org/10.1016/j.cirp.2019.04.070
12 S. Coraluppi and C. Carthel: Proc. 14th Int. Conf. Information Fusion (2011). https://ieeexplore.ieee.org/document/5977641
13 J. Martinez-del Rincon, C. Orrite-Urunuela, and J. E. Herrero-Jaraba: Proc IEEE Conf. Advanced Video and Signal Based Surveillance (2007) 176. https://doi.org/10.1109/AVSS.2007.4425306
14 S. Bashi, V. P. Jilkov, X. R. Li, and H. Chen: Proc. 6th Int. Conf. Information Fusion (2003) 1164. https://doi.org/10.1109/ICIF.2003.177369
15 M. Coates: Proc. 3rd Int Symp. Information Processing in Sensor Networks (2004) 99. https://doi.org/10.1145/984622.984637
16 D. Gu: Proc. 2007 IEEE Int Conf. Robotics and Automation (2007) 3856. https://doi.org/10.1109/ROBOT.2007.364070
17 M. Morbee, L. Tessens, H. Aghajan, and W. Philips. Electron. Lett. **46** (2010) 341. https://doi.org/10.1049/el.2010.0105
18 F. Castanedo, M. A. Patricio, J. García, and J. M. Molina: Proc. IEEE Conf. Advanced Video and Signal Based Surveillance (2007) 93. https://doi.org/10.1109/AVSS.2007.4425292
19 F. Castanedo, J. García, M. A. Patricio, and J. M. Molina: Proc. 11th Int. Conf. Information Fusion (2008). https://doi.org/10.1109/ICIF.2008.4632357
20 M. A. Davenport, C. Hegde, M. F. Duarte, and R. G. Baraniuk: IEEE Trans. Image Process **19** (2010) 2580. https://doi.org/10.1109/TIP.2010.2052821

About the Authors

Kun-Ying Li was born in Chiayi, Taiwan, in 1979. He received his B.S. degree from the Department of Bio Mechatronics Engineering, National Chung Hsing University and his M.S. degree from the Department of Mechanical Engineering, National Chung Cheng University, Taiwan, in 2007. From 2007 to 2020, he was an engineer with the Intelligent Machinery Technology Center in ITRI. He received his Ph.D. degree from National Chin-Yi University of Technology, Taiwan, in 2020. He has been an assistant professor in the Intelligent Automation Engineering Department at National Chin-Yi University of Technology since 2020. His research interests include thermal errors of machine tools and design for precision machinery, reliability engineering, and applications. He holds 15 patents in machine tools. (likunying@ncut.edu.tw)

Meng-Chiou Liao was born in Yunlin, Taiwan in 1985. She obtained a master's degree from the Institute of Engineering Science, National Cheng Kung University, Taiwan, in 2007. Her research interests are in digital signal processing and machine vision application technology.
(learn20200106@gmail.com)

Swami Nath Maurya received his B. Tech degree from the Department of Instrumentation and Control Engineering, Bundelkhand University (BU), Jhansi, India, in 2011 and his M. Tech degree from the Department of Green Energy Technology, Pondicherry University (PU), Puducherry, India, in 2015. He spent more than six years in different Indian solar industry companies. He is currently pursuing a Ph.D. degree from the Graduate Institute of Precision Manufacturing, National Chin-Yi University of Technology, Taiwan. His research interests include thermal errors of machine tools, solar energy, renewable energy, energy saving, sensors, and artificial intelligence. (smaurya077@gmail.com)